The Meshless Local Petrov–Galerkin Method in Two-Dimensional Electromagnetic Wave Analysis

Williams L. Nicomedes, Renato Cardoso Mesquita, and Fernando José da Silva Moreira, *Member, IEEE*

***Abstract*—This paper deals with one member of the class of meshless methods, namely the Meshless Local Petrov–Galerkin (MLPG) method, and explores its application to boundary-value problems arising in the analysis of two-dimensional electromagnetic wave propagation and scattering. This method shows some similitude with the widespread finite element method (FEM), like the discretization of weak forms and sparse global matrices. MLPG and FEM differ in what regards the construction of an unstructured mesh. In MLPG, there is no mesh, just a cloud of nodes without connection to each other spread throughout the domain. The suppression of the mesh is counterbalanced by the use of special shape functions, constructed numerically. This paper illustrates how to apply MLPG to wave scattering problems through a number of cases, in which the results are compared either to analytical solutions or to those provided by other numerical methods.**

***Index Terms*—Electromagnetic wave propagation, finite element method (FEM), integral equations, meshless methods.**

I. Introduction

MESHLESS (or meshfree) methods comprise a large class of numerical procedures whose seminal feature is, as the name indicates, the ability to provide numerical solutions to differential equations *without* the need of setting up any kind of mesh or grid in the geometrical domain where the problem is stated. There are resemblances with the finite element method (FEM), to which meshfree methods aim to be an alternative. The most patent ones are the following: the operation with weak forms (the differential equation is converted into an integral expression involving the function to be approximated and test functions), the use of compactly supported shape (or basis) functions, and the integration of the weak forms in local domains, which leads to global sparse matrices. Here, the concept of element loses its meaning. The classical idea of an element with its "connectivity array" linking nodes to edges is totally absent from the meshless approach. These methods present a more simplistic scenario, in which only a simple cloud of nodes spread throughout the domain is necessary.

The first studies concerning the use of meshfree techniques were reported in the early past decade, and many challenges concerning them remain to be studied [1]. They have successfully been applied in computational mechanics, and their use in areas such as elastostatics and hydrodynamics is very well developed. In computational electromagnetics, otherwise, meshfree techniques are still far from the spotlight. There are works based on partition of unity methods (PUM), such as the Method of Overlapping Patches [2] and the Generalized Finite Element Method (GFEM) [3]. PUM is a general technique that can be used in mesh-based methods (like the GFEM) and in meshless ones as well (like the Method of Overlapping Patches). A disadvantage of their use is the linear dependence and bad matrix condition numbers that can arise in the resulting equations [4], which can be circumvented by a redefinition of the basis functions so that they are orthogonal [3].

In some works [5]–[7], the Element-Free Galerkin (EFG) method has been employed. However, EFG is not regarded as a truly meshless method because background cells are necessary to perform the numerical integrations [1].

The Meshless Local Petrov–Galerkin (MLPG) method, unlike EFG, is a truly meshless method, in which the numerical integrations are carried out within certain local domains, which dismisses the use of any kind of background cells. MLPG was devised by S. Atluri within the framework of mechanics [8] and employs two kinds of functions, *shape functions* and *test functions*, which belong to two different function spaces. The shape functions are constructed numerically through procedures common to other meshless methods, whereas there are many choices available to the test functions. There are reports on the application of MLPG5 (the test function is a Heaviside function) to solve 2-D electrostatic problems [9]. Soares Jr. also solves problems concerning electromagnetic wave propagation in time domain through MLPG, in which two choices for the test function have been taken: Heaviside step functions and Gaussian weight functions [10]. Yu and Chen, otherwise, devise a meshless method whose formulation is quite different from MLPG: They employ a type of collocation procedure based on radial point interpolation (RPIM) shape functions in order to solve time-domain electromagnetic problems [11], [12]. Collocation procedures are attractive because there are no integrations. However, the nodal distribution employed in the aforementioned papers is based on a Voronoi decomposition, which makes the claim they are entirely meshless methods somehow hard to accept. We are particularly interested in MLPG4, whose test function is a solution to Green's problem

Manuscript received August 24, 2010; revised November 29, 2011; accepted December 02, 2011. Date of publication February 03, 2012; date of current version April 06, 2012. This work was supported in part by FAPEMIG, Brazil, under Grants Pronex TEC 01075/09 and TEC-APQ-00852-08 and CAPES, Brazil, under Grant RH-TVD-254/2008.

W. L. Nicomedes and F. J. S. Moreira are with the Department of Electronics Engineering, Federal University of Minas Gerais, Belo Horizonte MG 31270-901, Brazil (e-mail: wlnicomedes@yahoo.com.br; fernandomoreira@ufmg.br).

R. C. Mesquita is with the Department of Electrical Engineering, Federal University of Minas Gerais, Belo Horizonte MG 31270-901, Brazil (e-mail: renato@ufmg.br).

Color versions of one or more of the figures in this paper are available online at http://ieeexplore.ieee.org.

Digital Object Identifier 10.1109/TAP.2012.2186223

for Laplace's equation (reasons behind this choice will be addressed in Section IV). MLPG4 is also known as Local Boundary Integral Equation (LBIE) method. This method has been applied to 2-D electromagnetic wave scattering in [13], although the formalism developed there is not as general as the one that will be presented in this paper.

MLPG4/LBIE proved to be a reliable method, and we have been able to even blend it with an integral formulation [14]. The method has been employed in the determination of the band structure of photonic band-gap crystals [15]. Three-dimensional problems have also been attacked in electrostatics [16] and quantum mechanics [17].

The ideas presented in this paper unfold as follows. First, we give a general overview on meshless methods (Section II) and show how the shape functions are defined (Section III). Second, there follows a thorough description of LBIE, discussing the basic formulation in the frequency domain, weak forms, imposition of boundary conditions, and the treatment of material discontinuities (Section IV). Third, we take a look at the discretization process (Section V) and then proceed to discuss numerical details like integration quadratures, error norms, and the effect of imposing boundary conditions through the collocation method (Section VI). Section VII is devoted to illustrative examples showing how LBIE performs in several problems coming from classical electrodynamics.

II. Meshless Approach

Let Ω be a two-dimensional domain (whose global boundary is $\partial\Omega$) in which a given differential equation is to be solved. In order to find a numerical approximation u^h for a function u, which stands for the solution of the differential equation, we begin by spreading nodes across the domain. The nodal distribution need not be uniform (even random distributions can be used). A common practice employed to achieve better results is to increase the nodal density where the solution is expected to vary rapidly or near sharp edges. The next step is to define shape functions associated to each node. These functions do not have analytical expressions, demanding a numerical scheme to be constructed (as addressed in Section III). Usually, a shape function associated to a node depends on the relative positions of neighboring nodes. Furthermore, shape functions are compactly supported, i.e., they are different from zero only in a small region surrounding the node (called the node's *influence domain* Λ). It is this very property that renders the global matrix sparse. Thus, the collection of all shape functions ϕ_n (n runs from 1 to the total number of nodes N) forms a set $\mathcal{S}$ of two-dimensional compactly supported functions whose elements will be used to approximate u, i.e., given a point $\vec{x} = (x, y)$ where u^h shall be calculated (Fig. 1), there follows

$$u(\vec{x}) \sim u^h(\vec{x}) = \sum_{i=1}^{P} \phi_{c(i)}(\vec{x})\widehat{u}_{c(i)} = \boldsymbol{\Phi}(\vec{x})\widehat{\boldsymbol{u}}$$
$$\phi_{c(i)} \in \mathcal{S}, \qquad i = 1, 2, \ldots, P \tag{1}$$

where the global index $c(i)$ runs through all P nodes whose influence domains include point $\vec{x}$ (in Fig. 1, $c(1) = 3$, $c(2) = 7$, $c(3) = 9$, $c(4) = 17$, $c(5) = 20$; hence it follows that there are $P = 5$ influencing nodes) and each $\hat{u}_{c(i)}$ is a coefficient

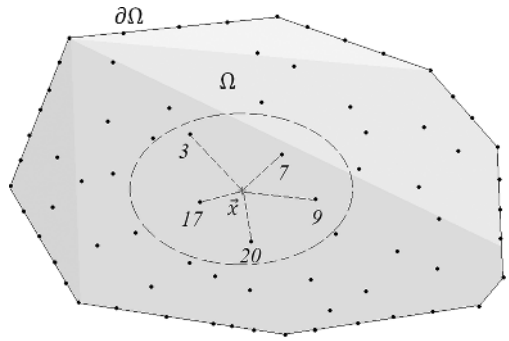

Fig. 1. Computational domain Ω, its global boundary $\partial\Omega$, and five nodes acting on point $\vec{x}$.

that must be determined (also called *nodal parameter*). When spreading the nodes, one constraint must be satisfied: The union of the influence domains from all nodes must cover the whole computational domain Ω

$$\Omega \subseteq \bigcup_{i=1}^{N} \Lambda_i. \tag{2}$$

Expression (2) means that no *holes* can be left behind, in order to ensure the approximation u^h everywhere inside the domain. The size of the influence domains can be adjusted, but should not be set too large, otherwise many nodes are able to extend their influence domains until $\vec{x}$, which could lead to more populated global matrices. Overlapping of influence domains is freely allowed.

We assume all influence domains Λ to be circles with the same radius r_0. That is not mandatory; one is free to choose any form and size, although simpler ones are easier to deal with. For example, in this paper we relied on a KdTree-based searching procedure to determine the closest nodes to a given point $\vec{x}$. From all nodes returned by the search, in order to find out if a node i extends its influence domain until $\vec{x}$, it suffices to verify if $\|\vec{x} - \vec{x}_i\| \leq r_0$.

III. Shape Functions: The MLS Approximation

The construction of the shape functions has been carried out through the Moving Least Squares (MLS) approximation [1]. In MLS, u^h at a point $\vec{x}$ is expressed as

$$u^h(\vec{x}) = \sum_{j=1}^{m} p_j(\vec{x})a_j(\vec{x}) = \boldsymbol{p}^T(\vec{x})\boldsymbol{a}(\vec{x}) \tag{3}$$

where $\boldsymbol{p}$ is a monomial basis with m terms (e.g., $\boldsymbol{p}^T = [1, x, y]$ for $m = 3$, which can be augmented in order to account for quadratic, cubic terms, etc.) and $\boldsymbol{a}$ is a vector of coefficients (to be determined soon) that are functions of $\vec{x}$. A slightly different approximation is then built by requiring the monomial basis to be calculated at each node $c(i)$ located at $\vec{x}_{c(i)}$

$$u^h\left(\vec{x}, \vec{x}_{c(i)}\right) = \sum_{j=1}^{m} p_j\left(\vec{x}_{c(i)}\right) a_j(\vec{x}) = \boldsymbol{p}^T\left(\vec{x}_{c(i)}\right)\boldsymbol{a}(\vec{x}). \tag{4}$$

The next step is to define a weighted functional M, which is a sum of squared differences between $u^h(\vec{x}, \vec{x}_{c(i)})$ and the nodal

parameter $\hat{u}_{c(i)}$, multiplied by a window function w centered at $\vec{x}_{c(i)}$ ($c(i)$ runs through all P nodes whose influence domains include point $\vec{x}$, like nodes 3, 7, 9, 17, and 20 in Fig. 1)

$$M = \sum_{i=1}^{P} w\left(\frac{\left\|\vec{x}-\vec{x}_{c(i)}\right\|}{r_{c(i)}}\right)\left[\sum_{j=1}^{m} p_j\left(\vec{x}_{c(i)}\right) a_j(\vec{x}) - \widehat{u}_{c(i)}\right]^2 \tag{5}$$

where $r_{c(i)}$ is the radius of the influence domain $\Lambda_{c(i)}$ associated to node $c(i)$ and w is (for other choices, see [1])

$$w(t) = \begin{cases} 1-6t^2+8t^3-3t^4, & 0 \le t \le 1 \\ 0, & \text{otherwise.} \end{cases} \tag{6}$$

Solving for the coefficients a_j that minimize M, we impose $\partial M/\partial a_j = 0$ for each a_j. After some extensive matrix manipulations, one arrives at

$$\boldsymbol{a}(\vec{x}) = [\boldsymbol{A}(\vec{x})]^{-1}[\boldsymbol{B}(\vec{x})]\,\widehat{\boldsymbol{u}} \tag{7}$$

where

$$\widehat{\boldsymbol{u}}^T = \left[\widehat{u}_{c(1)}, \widehat{u}_{c(2)}, \ldots, \widehat{u}_{c(P)}\right] \tag{8}$$

$$\boldsymbol{A}(\vec{x}) = \boldsymbol{P}^T\boldsymbol{W}(\vec{x})\boldsymbol{P} \tag{9}$$

$$\boldsymbol{B}(\vec{x}) = \boldsymbol{P}^T\boldsymbol{W}(\vec{x}) \tag{10}$$

which are given in terms of $\boldsymbol{P}$ and $\boldsymbol{W}$

$$\boldsymbol{P} = \begin{bmatrix} p_1\left(\vec{x}_{c(1)}\right) & \cdots & p_m\left(\vec{x}_{c(1)}\right) \\ \vdots & \ddots & \vdots \\ p_1\left(\vec{x}_{c(P)}\right) & \cdots & p_m\left(\vec{x}_{c(P)}\right) \end{bmatrix} \tag{11}$$

$$\boldsymbol{W}(\vec{x}) = \begin{bmatrix} w\left(\frac{\left\|\vec{x}-\vec{x}_{c(1)}\right\|}{d_{c(1)}}\right) & \cdots & 0 \\ \vdots & \ddots & \vdots \\ 0 & \cdots & w\left(\frac{\left\|\vec{x}-\vec{x}_{c(P)}\right\|}{d_{c(P)}}\right) \end{bmatrix}. \tag{12}$$

The shape functions are then obtained by equating (1) to (3)

$$\boldsymbol{\Phi}(\vec{x}) = \left[\phi_{c(1)}(\vec{x}), \ldots, \phi_{c(P)}(\vec{x})\right] = \boldsymbol{p}^T\boldsymbol{A}^{-1}(\vec{x})\boldsymbol{B}(\vec{x}). \tag{13}$$

Fig. 2 shows a simple MLS shape function ϕ associated to a node and its derivatives. From Fig. 2, one sees that ϕ is smooth, even if a linear basis $\boldsymbol{p}$ is employed, thanks to the window function w. This is a great advantage when calculating the derivatives of u^h. Another feature is that MLS shape functions do not satisfy the Kronecker delta property, i.e., $\phi_i(\vec{x}_j) \neq \delta_{ij}$. In order to calculate the derivatives of the shape functions, more matrix calculations are necessary [1]

$$\boldsymbol{\Phi}_q(\vec{x}) = \boldsymbol{\gamma}_q^T(\vec{x})\boldsymbol{B}(\vec{x}) + \boldsymbol{\gamma}^T(\vec{x})\boldsymbol{B}_q(\vec{x}) \tag{14}$$

where the subscript q represents a partial derivative with respect to x or y (i.e., $q = x$ or $q = y$). The vector $\boldsymbol{\gamma}$ in (14) is found through $\boldsymbol{A}(\vec{x})\boldsymbol{\gamma}(\vec{x}) = \boldsymbol{p}(\vec{x})$.

IV. Local Boundary Integral Equation Method

We now proceed to lay down the mechanism of MLPG4/LBIE. The approach herein developed differs from that presented in [8], [13], and [14], especially in what concerns the imposition of boundary conditions. We took some ideas regarding the treatment of interface conditions from [18]. In [16] and [17], we applied to three-dimensional situations the very same approach described in this paper, which proved to be reliable and efficient. The illustrative examples will be taken from the analysis of two-dimensional electromagnetic wave scattering. Throughout the development, it is assumed that no parameter depends on the z-direction; thus $\partial/\partial z = 0$. Besides that, the fields are assumed to be time-harmonic (variation $e^{j\omega t}$). Thus, the characteristic equation to be dealt with is the inhomogeneous Helmholtz equation

$$\nabla\cdot\left(\frac{1}{p(\vec{x})}\nabla u^h(\vec{x})\right) + k_0^2 q(\vec{x}) u^h(\vec{x}) = f(\vec{x}). \tag{15}$$

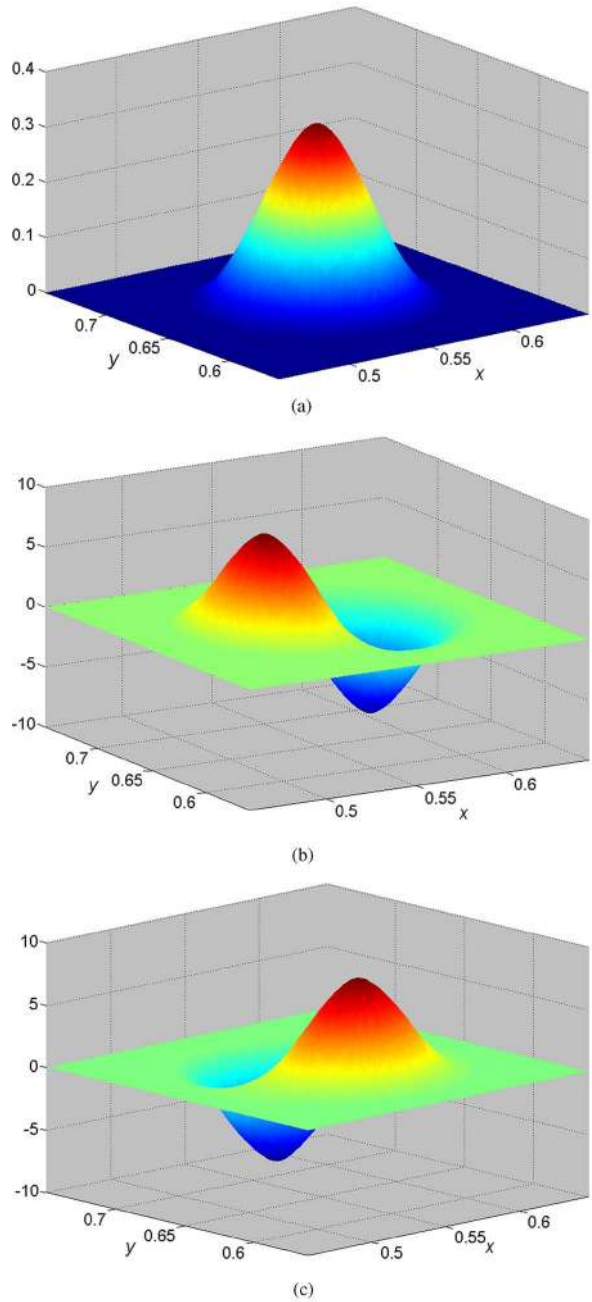

Fig. 2. MLS shape function associated to a node located at (0.55, 0.65). (a) Shape function ϕ. (b) Its derivative with respect to x, $\partial\phi/\partial x$. (c) Its derivative with respect to y, $\partial\phi/\partial y$.

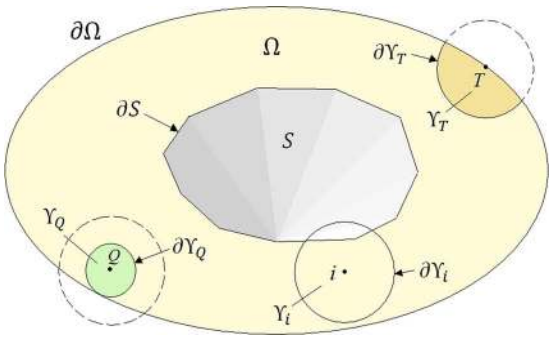

Fig. 3. Scatterer S within the computational domain $\partial\Omega$. Node i: $r_i = s_i$. Node Q: $r_Q \neq s_Q$. The shadowed region Υ_T (boundary $\partial\Upsilon_T$) is the test domain that would be assigned to the boundary node T if an intersection had to be found out first.

For TM^z polarization, u^h is the z-component of the electric field E_z, p is the relative magnetic permeability μ_r, and q is the relative electric permittivity ε_r. For TE^z polarization, u^h is the z-component of the magnetic field H_z, p is the relative electric permittivity ε_r, and q is the relative magnetic permeability μ_r. In both cases, k_0 is the free-space wavenumber ($k_0 = 2\pi/\lambda_0$, λ_0 is the free-space wavelength), and f is the source term.

Let S be a scatterer (boundary ∂S) whose properties $p(\vec{x})$ and $q(\vec{x})$ are functions of position $\vec{x}$. In order to apply MLPG4, we must consider also a free-space layer surrounding S; the global boundary $\partial\Omega$ is placed away from the surface of the scatterer. Hence, the computational domain is Ω, in which p and q are set equal to 1 in the free-space region outside ∂S and vary smoothly with $\vec{x}$ inside ∂S (Fig. 3). We begin by spreading nodes across the computational domain. The nodes inside Ω are called the *interior nodes*, and those located exactly at $\partial\Omega$ are the *boundary nodes*. To each node i (interior and boundary nodes as well), a shape function is associated, whose compact support Λ_i is a circle with radius r_i. In addition to the shape function, another function, called the *test function*, is associated *to interior nodes only*. This test function v_i acts in a specific region surrounding the node, called the node's *test domain* and represented by Υ_i (Fig. 3). In LBIE, the test domain is required to be a *circle* centered at each interior node i. Other requirements that must be satisfied by the function v_i are

$$\begin{aligned} &\nabla^2 v_i = -\delta(\vec{x} - \vec{x}_i) \text{ (a Dirac delta at } \vec{x}_i) \\ &\quad v_i = 0 \text{ at the boundary } \partial\Upsilon_i \text{ of the test domain } i \end{aligned} \tag{16}$$

The function v_i satisfying the above requirements is

$$v_i(\vec{x}) = \frac{1}{2\pi} \ln\left(\frac{s_i}{\|\vec{x} - \vec{x}_i\|}\right) \tag{17}$$

where s_i is the radius of test domain Υ_i. In general, for an interior node, the radii r_i and s_i are different from each other, as will be explained.

The test domains are the regions in which the integrations are carried out. The simpler in form they are, the simpler it becomes to employ the numerical quadratures. In what regards boundary nodes, if circular test domains were ascribed to them, an intersection between the global domain Ω and the circle Υ_i would have to be found in order to carry out the numerical integration. Fig. 3 shows this: Had a test domain been assigned to node T, then the numerical integration would have to be performed in the shaded region. However, trying to find intersections between curves is too cumbersome and hinders the whole process (we actually did it in [13] and [14]). This is the main reason why the approach that uses test domains for boundary nodes was dismissed in favor of the more efficient one described in this paper (Section IV-B). Thus, boundary nodes have no associated test domains at all.

To avoid the intersection between the test domain Υ_i associated to an interior node i and the global boundary $\partial\Omega$ (i.e., $\Upsilon_i \cap \partial\Omega = \emptyset$), the test domain radius s_i is chosen as

$$s_i = \min\{r_i, d_i\} \tag{18}$$

where d_i is the distance between the interior node i at $\vec{x}_i$ and $\partial\Omega$. This procedure ensures that if the interior node is too close to the global boundary, the associated test domain is chosen so that it just touches $\partial\Omega$ (node Q in Fig. 3). An interior node is then characterized by four parameters (the two coordinates x_i and y_i, the radius of its influence domain r_i, and the radius of its test domain s_i), whereas a boundary node is characterized by three parameters only (x_i, y_i, and r_i).

Now that both shape and test functions have been defined, we proceed to get the weak form for (15). There are two ways through which this task can be accomplished: One of them uses the weighted residual method, and the other uses Green's second identity. The latter leads directly to boundary integral equations, which lie at the core of LBIE method, and as such, will be presented in what follows.

A. Green's Second Identity and Local Boundary Integral Equations

This approach is valid only in regions where the function $p(\vec{x})$ is a constant (for example, in problems where p is constant throughout the domain Ω or in each of the subregions of Ω where p is piecewise constant). If p is constant, then (15) can be written as

$$\nabla^2 u^h + k_0^2 pq u^h = fp. \tag{19}$$

Now one takes Green's second identity for the two functions u^h and v_i, and then performs the integrations in the test domain Υ_i (and at its boundary $\partial\Upsilon_i$) for each interior node i

$$\iint_{\Upsilon_i} (u^h \nabla^2 v_i - v_i \nabla^2 u^h) dS = \oint_{\partial\Upsilon_i} \left(u^h \frac{\partial v_i}{\partial n} - v_t \frac{\partial u^h}{\partial n}\right) dl. \tag{20}$$

As $\nabla^2 v_i = -\delta(\vec{x} - \vec{x}_i)$ and $v_i = 0$ at the boundary $\partial\Upsilon_i$ [from (16)], and taking $\nabla^2 u^h$ from (19), one arrives at the following expression:

$$u^h(\vec{x}_i) + \oint_{\partial\Upsilon_i} u^h \frac{\partial v_i}{\partial n} dl - \iint_{\Upsilon_i} k_0^2 pq u^h v_i dA = -\iint_{\Upsilon_i} fp v_i dA \tag{21}$$

where $u^h(\vec{x}_i)$ is the value of u^h evaluated at $\vec{x}_i$, the location of the interior node i. It is due to weak forms disguised under the form of boundary integral equations that the method described

in this paper also bears the name of Local Boundary Integral Equation (LBIE) method.

B. Imposing Boundary Conditions

The information concerning the boundary conditions at $\partial\Omega$ comes into the problem through the boundary nodes (which, according to Section IV, have no associated test domains). The boundary conditions are therefore imposed by a *meshless collocation* scheme, based on the approximation described by (1). Let us suppose that a node m (coordinates $\vec{x}_m = (x_m, y_m)$) lies at a portion of the global boundary $\partial\Omega$ where the boundary conditions are expressed in general form as

$$a(\vec{x})u(\vec{x}) + b(\vec{x})\frac{\partial u(\vec{x})}{\partial n} = g(\vec{x}) \tag{22}$$

where $a(\vec{x})$ and $b(\vec{x})$ are given functions of the position $\vec{x}$ along $\partial\Omega$, and $g(\vec{x})$ is a known function of $\vec{x}$. In (22), three types of boundary conditions are embedded. If Dirichlet conditions are to be imposed, then $a(\vec{x}) = 1$ and $b(\vec{x}) = 0$. In the case of Neumann conditions, then $a(\vec{x}) = 0$ and $b(\vec{x}) = 1$. In treating Robin conditions, $a(\vec{x}) \neq 0$ and $b(\vec{x}) \neq 0$. Hence, based on the approximation (1), and for a boundary node located at $\vec{x} = \vec{x}_m$, there follows

$$a(\vec{x}_m)u^h(\vec{x}_m) + b(\vec{x}_m)\frac{\partial u^h(\vec{x}_m)}{\partial n} = g(\vec{x}_m). \tag{23}$$

Expanding (23), we have a nodal equation

$$a(\vec{x}_m)\sum_{i=1}^{Q}\phi_{c(i)}(\vec{x}_m)\widehat{u}_{c(i)} + b(\vec{x}_m)\sum_{i=1}^{Q}\frac{\partial\phi_{c(i)}(\vec{x}_m)}{\partial n}\widehat{u}_{c(i)} = g(\vec{x}_m) \tag{24}$$

where the global index $c(i)$ runs through all Q nodes whose influence domains include point $\vec{x}_m$ (in Fig. 4, $Q = 5$ and the global indices are $c(1) = 2$, $c(2) = 5$, $c(3) = 21$, $c(4) = 30$, and $c(5) = m$. Since the distance from node m to $\vec{x}_m$ is zero, the window function w centered at $\vec{x}_m$ is exactly 1 at $\vec{x}_m$), $\phi_{c(i)}(\vec{x}_m)$ is the shape function associated to the influencing node $c(i)$ evaluated at the point $\vec{x}_m$, $\partial\phi_{c(i)}(\vec{x}_m)/\partial n$ is the normal derivative of the shape function associated to node $c(i)$ evaluated at $\vec{x}_m$, and $\hat{u}_{c(i)}$ is the nodal parameter associated to node $c(i)$ (unknown). This meshless collocation procedure enforces the boundary conditions in a fairly simple way—neither finding intersections between domains nor performing numerical integrations is necessary.

C. Handling Material Discontinuities

Care must be taken when dealing with problems in which some material property [described by the function $p(\vec{x})$ in (15)] is discontinuous across an interface. This is so because the shape functions are smooth (i.e., the functions themselves and their derivatives are continuous). Shape functions inherit the order of continuity from the window function (in this work, a $C^4(\Lambda)$ function, Λ being the nodal influence domain). In electromagnetic wave scattering analysis, when the unknown function u is the electric field E_z (TM^z polarization) and when there are no magnetic materials inside the domain Ω ($p(\vec{x}) = \mu_{\mathrm{r}}(\vec{x}) = 1$ everywhere), one knows that the normal derivative $\partial E_z/\partial n$ must

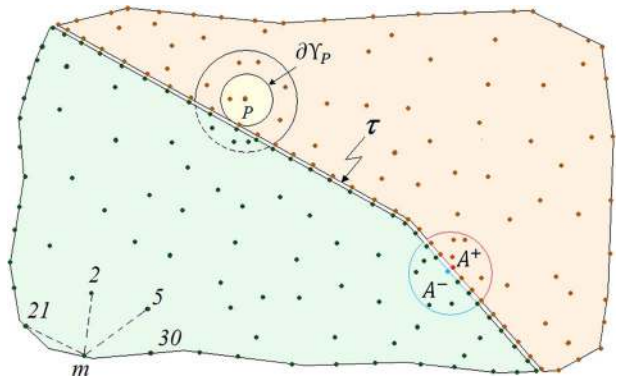

Fig. 4. Computational domain in which there is a material discontinuity at the interface τ. A double layer of nodes is placed along τ. A^- and A^+ are dual nodes. The boundary $\partial\Upsilon_P$ of test domain associated to node P just touches the interface τ. The nodes inside its influence domain *and located at the other side of* τ (inside the dashed portion of the larger circumference centered at P) are not influenced by P.

be continuous across the interface between two dielectric media ($q(\vec{x}) = \varepsilon_{\mathrm{r}}^-$ at one side and $q(\vec{x}) = \varepsilon_{\mathrm{r}}^+$ at the other side). This poses no problem when expressing the electric field as an expansion like (1) because the shape functions are known to be smooth and thus able to reproduce the continuity of $\partial E_z/\partial n$. However, there is a small issue when it comes to TE^z polarization: The magnetic field H_z experiences a discontinuity in its normal derivative across the interface between two dielectric media

$$\frac{1}{\varepsilon_{\mathrm{r}}^-}\frac{\partial H_z^-}{\partial n} = \frac{1}{\varepsilon_{\mathrm{r}}^+}\frac{\partial H_z^+}{\partial n} \tag{25}$$

where H_z^- is the magnetic field at one side of the interface and H_z^+ is the field at the other side. The function $p(\vec{x}) = \varepsilon_{\mathrm{r}}(\vec{x})$ is discontinuous across an interface, and there is not a direct way of inserting (25) in the governing equation (15). If one tries to solve (15) without giving this issue its due attention, only an approximate solution for H_z will be obtained (smoother than the real one) since the shape functions used to represent the magnetic field are smooth and thus unable to reproduce a discontinuity such as (25). In order to deal with material discontinuities in TE^z polarization, we employ a technique described in [18].

Let us assume a relative permittivity ε_{r} that is piecewise homogeneous: Each subregion i has a relative permittivity $\varepsilon_{\mathrm{r}_i}$. In Fig. 4, there are two such subregions, each one with its relative permittivity, separated by an interface τ. Nodes from one region are required not to influence the other, even if theoretically their influence domains could extend over there (in Fig. 4, node P lies in region 2, so nodes from region 1 lying inside the dashed curve are not influenced by this node, even if they are located within the influence domain of P). Moreover, the test domains assigned to interior nodes from one region just touch the interface τ (interior circle associated to node P). Now, in addition to interior nodes and to boundary nodes, this situation demands a new kind of node: an *interface node*. Along the interface τ is placed a double layer of nodes, i.e., nodes lying at the interface are doubled: Each interface node is actually considered equivalent to two nodes, one belonging to region 1 and the other to region 2. Each interface node has its dual; they are placed at

exactly the same location, but are two distinct entities, to each one being assigned a nodal parameter $\hat{u}$ and thus a row in the global matrix (Fig. 4, nodes A^- and A^+). A restriction is then imposed: Node A^- influences (and is influenced by) only nodes from region 1; node A^+ influences (and is influenced by) only nodes from region 2. No test domains are assigned to interface nodes: A meshless collocation scheme, like that one described in Section IV-B, is enforced at each dual-interface node, one dealing with interface conditions on the function itself (u^h) and the other with conditions on the normal derivative ($\partial u^h/\partial n$). In TE^z analysis, the interface conditions are

$$\begin{aligned} H_z^- = H_z(A^-) = H_z(A^+) = H_z^+ \\ \therefore \sum_{i=1}^{N_1} \phi_{c(i)}(A^-)\widehat{u}_{c(i)} = \sum_{j=1}^{N_2} \phi_{c(j)}(A^+)\widehat{u}_{c(j)} \end{aligned} \tag{26}$$

$$\begin{aligned} \frac{1}{\varepsilon_{\mathrm{r}}^-}\frac{\partial H_z^-}{\partial n} = \frac{1}{\varepsilon_{\mathrm{r}}^-}\frac{\partial H_z(A^-)}{\partial n} = \frac{1}{\varepsilon_{\mathrm{r}}^+}\frac{\partial H_z(A^+)}{\partial n} = \frac{1}{\varepsilon_{\mathrm{r}}^+}\frac{\partial H_z^+}{\partial n} \\ \therefore \frac{1}{\varepsilon_{\mathrm{r}}^-}\sum_{i=1}^{N_1}\frac{\partial \phi_{c(i)}(A^-)}{\partial n}\widehat{u}_{c(i)} = \frac{1}{\varepsilon_{\mathrm{r}}^+}\sum_{j=1}^{N_2}\frac{\partial \phi_{c(j)}(A^+)}{\partial n}\widehat{u}_{c(j)} \end{aligned} \tag{27}$$

where the global index $c(i)$ runs through all N_1 nodes from region 1 whose influence domains include point A^- (in Fig. 4, they are depicted inside the semicircle surrounding A^-), and $c(j)$ through all N_2 nodes from region 2 whose influence domains include point A^+ (nodes inside the semicircle surrounding A^+). Hence, through the collocation scheme, the interface conditions for TE^z polarization can be imposed without relying on any kind of numerical integration: Simple nodal equations such as (26) and (27) are able to impose the discontinuity condition expressed by (25).

V. LBIE Discretization

Let Ω be the computational domain in which the given differential equation (15) is to be solved. One begins by spreading nodes within Ω (the interior nodes) and along $\partial\Omega$ (the boundary nodes), where some kind of boundary condition is imposed. If that is the case of there being a curve τ separating two media, then along τ is placed a double layer of nodes, the interface nodes. After the nodal distribution is set up, one proceeds to evaluate the weak forms (21).

Suppose i is the global index for an interior node. After defining its circular test domain Υ_i [whose radius s_i is found through (18)], the next step is to express u^h as a weighted sum of shape functions, like (1), which is substituted in (21). As the nodal parameters $\hat{u}$ stand for the unknowns of the problem, this leads to a linear system, in a way quite similar to FEM

$$\boldsymbol{K}\widehat{\boldsymbol{u}} = \boldsymbol{F} \rightarrow \widehat{\boldsymbol{u}} = \boldsymbol{K}^{-1}\boldsymbol{F}. \tag{28}$$

The interaction between global nodes i and j is given by K_{ij}, i.e., the element located at row i and column j in the global matrix $\boldsymbol{K}$

$$K_{ij} = \phi_j(\vec{x}_i) + \oint_{\partial\Upsilon_i} \phi_j \frac{\partial v_i}{\partial n} dl - \iint_{\Upsilon_i} k_0^2 pq v_i \phi_j dA. \tag{29}$$

In (29), if the shape function ϕ_j associated to global node j does not extend its influence domain over some portion of the test domain Υ_i associated to global node i, then K_{ij} is obviously equal to zero. Because the shape functions are compactly supported, this will happen whenever nodes i and j are not close enough to each other. The global matrix is therefore sparse. Expression (29) is to be enforced at each interior node. The component F_i of the excitation vector $\boldsymbol{F}$ is

$$F_i = -\iint_{\Upsilon_i} f p v_i dS. \tag{30}$$

In what regards boundary nodes, let i be a global node located at $\partial\Omega$. From (24), one gets

$$K_{ij} = a(\vec{x}_i)\phi_j(\vec{x}_i) + b(\vec{x}_i)\frac{\partial \phi_j(\vec{x}_i)}{\partial n}, \quad F_i = g(\vec{x}_i). \tag{31}$$

The interface conditions are imposed through (26) and (27). Let it be an interface node whose global index is i (e.g. A^- in Fig. 4), and suppose that its dual has global index k (e.g. A^+ in Fig. 4). Then

$$K_{ij} = \phi_j(\vec{x}_i) - \phi_j(\vec{x}_k) \quad F_i = 0 \tag{32}$$

$$K_{kj} = \frac{1}{\varepsilon_{\mathrm{r}}^-}\frac{\partial \phi_j(\vec{x}_i)}{\partial n} - \frac{1}{\varepsilon_{\mathrm{r}}^+}\frac{\partial \phi_j(\vec{x}_k)}{\partial n} \quad F_k = 0. \tag{33}$$

It must be remembered that, as explained in Section IV, if the global node j is at the same side of the interface as $\vec{x}_i$, it influences only $\vec{x}_i$ (i.e., only A^-); it does not influence $\vec{x}_k$, i.e., $\phi_j(\vec{x}_k) = 0$ (it does not influence A^+). The same holds if node j is located at the same side of the interface as $\vec{x}_k$: It influences only $\vec{x}_k$ (i.e., only A^+); it does not influence $\vec{x}_i$, i.e., $\phi_j(\vec{x}_i) = 0$ (it does not influence A^-).

VI. Numerical Aspects

A. Integration of Weak Forms

One should observe that as the shape functions ϕ_j do not have analytical expressions, the integrals in (29) and (30) must be carried out numerically, usually through a Gaussian quadrature. Here lies the main drawback of MLPG: The more refined are the integrations of (29) and (30), the greater is the number of Gaussian points required. The cost of this reflects directly in the process of filling up the global matrix $\boldsymbol{K}$. Efficient ways of filling the global matrices are currently a topic of research [19], and a discussion about the impact of different approaches to the integration of weak forms on the overall performance of the MLPG procedure falls outside the scope of this paper. In this work, we employ a simple Gaussian quadrature. Let us consider the area integral first [third term of (29); (30) is treated in exactly the same way]. As the test domains are circles, "local" polar coordinates (ρ, φ) revealed to be extremely useful. We take a test domain Υ_i and divide it up into "cells," determined by lines of constant ρ and φ. If we represent each cell by Δ, we see that Υ_i is the union of a disjoint set of such cells

$$\Upsilon_i = \bigcup_m \bar{\Delta}_m \quad \Delta_m \cap \Delta_n = \emptyset \quad m \neq n. \tag{34}$$

The "local" polar coordinate system is centered at the node's location $\vec{x}_i$, and the conversion to rectangular coordinates is given by $x = x_i + \rho\cos(\varphi), y = y_i + \rho\sin(\varphi)$. The third term in (29) is treated as follows:

$$\iint_{\Upsilon_i} k_0^2 pq v_i \phi_j dA = \int_0^{s_i}\int_0^{2\pi} g(\rho,\varphi) d\varphi d\rho \tag{35}$$

where $g(\rho,\varphi) = k_0^2 pq v_i \phi_j \rho$. Each integration cell Δ_m is limited by radii ρ_m^1 and ρ_m^2 and by angles φ_m^1 and φ_m^1. Since the cells are disjoint, the integral in the right side of (35) can be substituted by a sum of integrals evaluated at each cell

$$\sum_m \iint_{\Delta_m} g(\rho,\varphi) d\varphi d\rho = \sum_m \int_{\rho_1^m}^{\rho_2^m}\int_{\varphi_1^m}^{\varphi_2^m} g(\rho,\varphi) d\varphi d\rho. \tag{36}$$

We applied a two-point Gaussian quadrature to ρ and φ in Δ_m (four Gaussian points per cell). Therefore

$$\int_{\rho_1^m}^{\rho_2^m}\int_{\varphi_1^m}^{\varphi_2^m} g(\rho,\varphi) d\varphi d\rho \cong \frac{(\rho_2^m - \rho_1^m)(\varphi_2^m - \varphi_1^m)}{4} \sum_{r=1}^{2}\sum_{s=1}^{2} w_r w_s g\left(\overline{\rho_r^m}, \overline{\varphi_s^m}\right) \tag{37}$$

where the coordinates of the Gaussian points are

$$\overline{\rho_r^m} = \frac{(\rho_2^m - \rho_1^m)}{2}\xi_r + \frac{(\rho_2^m + \rho_1^m)}{2} \tag{38}$$

$$\overline{\varphi_s^m} = \frac{(\varphi_2^m - \varphi_1^m)}{2}\xi_s + \frac{(\varphi_2^m + \varphi_1^m)}{2}. \tag{39}$$

The parameters for the two-point Gaussian quadrature are $w_1 = w_2 = 1$ and $\xi_1 = -1/\sqrt{3}$, $\xi_2 = 1/\sqrt{3}$. According to (17), the test function v_i has a singularity exactly at the location of node i (i.e., at $\vec{x}_i$, center of Υ_i). By dividing up Υ_i into cells in the way described above, we guarantee that no Gaussian point coincides with the center of Υ_i. To see why, suppose that Δ_m is a cell located in the innermost layer, i.e., $\rho_1^m = 0$ and $\rho_2^m \neq 0$. From (38), we see that there is no way in which $\overline{\rho_r^m}$ could be zero. In this paper, we employed 18 cells [$m = 18$ in (34)], which yields 72 Gaussian points per test domain.

The line integral [second term in (29)] is simpler to deal with, as ρ is constant (namely, the radius of the test domain s_i). Thus

$$\oint_{\partial\Upsilon_i} \phi_j \frac{\partial v_i}{\partial n} dl = \int_0^{2\pi} g(\varphi) d\varphi = \sum_m \int_{\Delta_m} g(\varphi) d\varphi \tag{40}$$

where $g = \phi_j(\partial v_i/\partial n)s_i$, and $\Delta_m = [\varphi_1^m, \varphi_2^m]$ are angular segments. We approximate the integrals in (40) as

$$\int_{\Delta_m} g(\varphi) d\varphi = \int_{\varphi_1^m}^{\varphi_2^m} g(\varphi) d\varphi \cong (\varphi_2^m - \varphi_1^m)\, g\left(\frac{\varphi_2^m + \varphi_1^m}{2}\right). \tag{41}$$

In solving the examples, we took 20 segments for each of the test domains [$m = 20$ in (40)].

B. Error Convergence

In order to determine the performance of MLPG4 when the number of nodes in Ω increases, we take a well-behaved Dirichlet problem: a TM^z uniform plane wave propagating in the x direction. Let us consider a square portion of free space Ω, and assume that we know the incident electric field E_z at all points of the boundary $\partial\Omega$. Since we are dealing with free space, the problem we are concerned with is

$$\begin{cases} \nabla^2 E_z + k_0^2 E_z = 0 \text{ in } \Omega \\ E_z = e^{-jk_0 x} \text{ at } \partial\Omega. \end{cases} \tag{42}$$

As there are neither sources (radiated fields) nor dielectric materials (scattered fields) within Ω, the electric field is undisturbed. Therefore, the solution to (42) is $E_z = e^{-jk_0 x}$ V/m for all points $\vec{x} \in \Omega$.

We now proceed to calculate the difference between the numerical and exact solutions. Given a nodal distribution over the computational domain Ω, we first find the discretization length h, calculated as the maximum internodal distance, i.e., for each node i we find the distance D_i to its closest neighbor node, thus forming a set $D = \{D_1, D_2, \ldots, D_N\}$, where N is the total number of nodes. The discretization length is the greatest element of D

$$D_i = \min_{\substack{1\le j\le N \\ j\neq i}} \{d_{ij}\} \quad h = \max\{D_1, D_2, \cdots, D_N\}. \tag{43}$$

After the solution of (42) for a given nodal distribution, we compute the relative error (ratio of the L^2 norm of the difference between the solutions to the L^2 norm of the exact solution)

$$\frac{\left\|E_z^{\mathrm{MLPG}} - E_z^{\mathrm{exact}}\right\|_2}{\left\|E_z^{\mathrm{exact}}\right\|_2} = \frac{\sqrt{\iint_\Omega \left|E_z^{\mathrm{MLPG}} - E_z^{\mathrm{exact}}\right|^2 dA}}{\sqrt{\iint_\Omega \left|E_z^{\mathrm{exact}}\right|^2 dA}}. \tag{44}$$

This procedure was carried out for populations whose number of nodes varies from 60 to approximately 3000. We took a 1-GHz incident plane wave, and Ω is a square whose side is given by 1λ. The same analysis has been extended to FEM [with first-order elements since the MLS shape functions employ a linear basis (3)], from whose meshes we took the nodal distributions and defined h as in (43). The result that shows how the error norm behaves as a function of h is shown in Fig. 5. A linear regression reveals the convergence rate to be 2.484 for MLPG4/LBIE and 1.791 for FEM. As the number of nodes increases and, consequently h decreases, the condition number of the global matrix varies from 34 to 940.

The codes regarding this and all other examples in this paper are implemented in MATLAB. Besides providing a friendly environment for developing numerical computations, MATLAB has a built-in matrix solver based on LU factorization with partial pivoting. The global linear systems (28) for all problems can therefore be solved directly; writing specific codes for solving linear systems is not among the tasks we have set up to accomplish in this work.

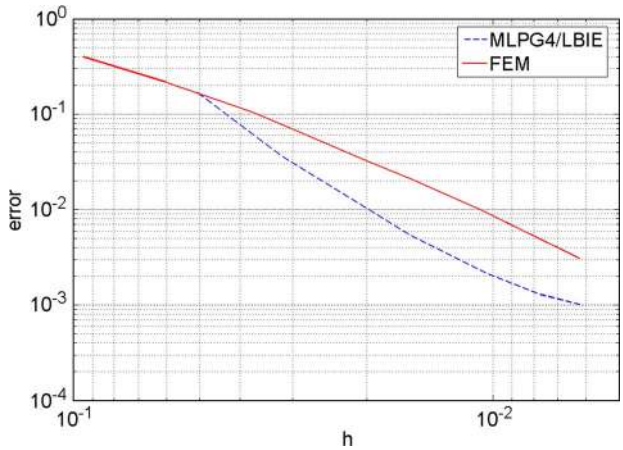

Fig. 5. Graph in logarithmic scale showing the relative errors for MLPG4/LBIE and FEM. The discretization length h is measured in meters.

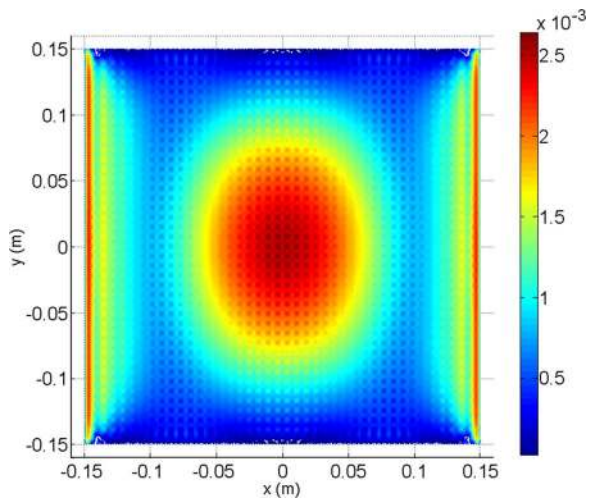

Fig. 6. Square computational domain Ω set up for problem (42): $[-0.15\ \text{m}, 0.15\ \text{m}]^2$ at 1 GHz. The graph depicts the absolute value of the difference between the MLPG4 and the exact solution $||E_z^{\text{MLPG}} - E_z^{\text{exact}}||$ for a total of 1760 nodes (40×40 nodes uniformly distributed within Ω, and 40 nodes at each one of the four edges).

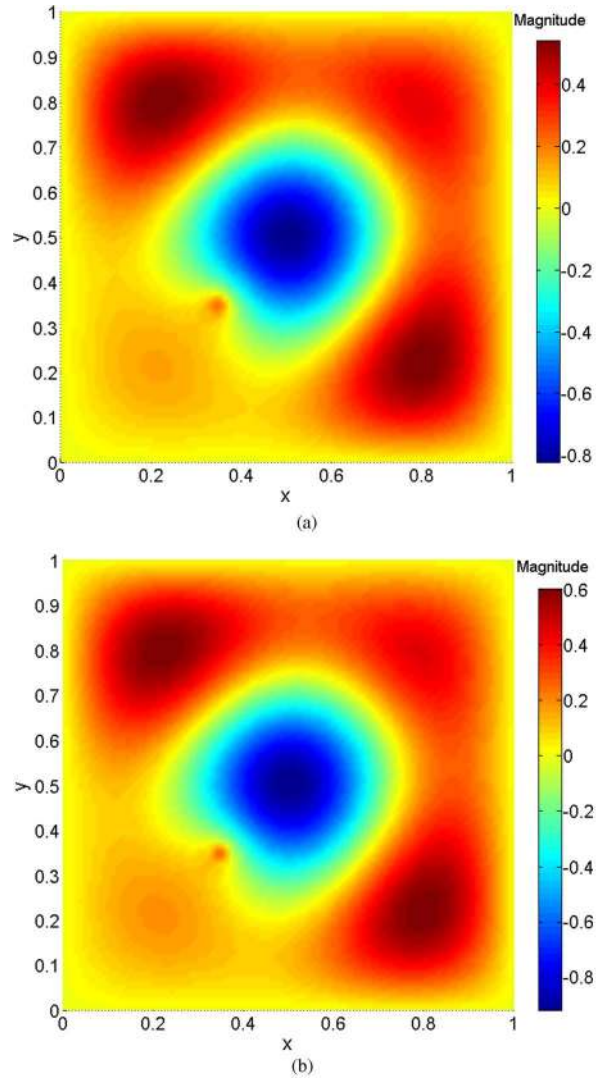

Fig. 7. First example (Green's problem): (a) MLPG4 numerical result and (b) the analytical solution.

C. Boundary Conditions and the Collocation Method

Not ascribing test domains to boundary nodes gives rise to tiny regions in Ω that are not covered by such domains, i.e., (2) does not hold when the influence domains Λ are replaced by the Υ's. These regions are so small that they can barely be noticed. Moreover, all points from the global boundary $\partial\Omega$ are uncovered by test domains (for the test domains of the interior nodes just touch $\partial\Omega$, as explained earlier in Section IV). To make sure that this issue has no significant influence on the precision of the results at the uncovered regions, Fig. 6 shows a comparison between the exact and the numerical solutions for problem (42) at all points in the computational domain Ω. The absolute value of the difference between the numerical and the exact solutions seems to distribute around the center of the domain (where no collocation procedure is used). Although this difference reaches a higher value near the left and right edges of Ω, on the other hand it assumes extremely low values near the top and bottom edges. Numerical experiments suggest that the collocation procedure is able to effectively impose the boundary conditions, insofar as the highest errors are attained in the central regions, away from the global boundary $\partial\Omega$.

VII. Numerical Examples

A. First Example: Green's Problem

The first example simulates the electric field E_z inside a cavity excited by a line of current, i.e., one is interested in Green's problem

$$\nabla^2 E_z + k_0^2 E_z = -\delta(x-\xi)\delta(y-\eta). \tag{45}$$

Equation (45) is to be solved inside a square region $\Omega = (0,1\ \text{m}) \times (0,1\ \text{m})$ where $k_0 = 10$ rad/m and the condition $E_z = 0$ is imposed along the global boundary $\partial\Omega$ (a perfect conductor). The current source is located at $(\xi, \eta) = (0.35\ \text{m}, 0.35\ \text{m})$. A total of 1796 nodes have been spread across the computational domain, and each node influences, approximately, 16 other nodes. Fig. 7 compares the analytical solution for this problem [20, Ch. 5] to the numerical

one provided by MLPG4/LBIE. The concordance is quite reasonable, as observed.

B. Second Example: TM Scattering

The second problem addresses the TM^z scattering of a plane wave by a dielectric circular cylinder. The electric incident field is $E_z^i = e^{-jk_0x}$, and the frequency is 1 GHz. The scatterer is modeled by a circle S (boundary ∂S, radius a) within which the relative permittivity is given. In order to deal with scattered fields, a first-order Bayliss–Turkel radiation boundary condition (RBC) is imposed at a circumference placed away from the scatterer [21]

$$\frac{\partial E_z^s}{\partial n} + \left(jk_0 + \frac{1}{2\rho_b}\right) E_z^s = 0 \tag{46}$$

where E_z^s is the scattered field and ρ_b is the radius of $\partial\Omega$. As explained in Section IV, there is a free-space layer between the scatterer surface ∂S and the circumference where the RBC is imposed, i.e., the global boundary $\partial\Omega$ ($\partial\Omega$ and ∂S are concentric circumferences). Because we employ a first-order RBC, the radius of $\partial\Omega$ was chosen three times larger than the radius of the scatterer ($\rho_b = 3a$). According to (15), the function $p(\vec{x}) = \mu_{\mathrm{r}}(\vec{x}) = 1$ everywhere, whereas $q(\vec{x}) = \varepsilon_{\mathrm{r}} = 1$ between $\partial\Omega$ and ∂S, and $q(\vec{x}) = \varepsilon_{\mathrm{r}}$ within ∂S. Besides that, the excitation term $f(\vec{x})$ is zero everywhere.

As we are interested in the total field E_z, we substitute $E_z = E_z^i + E_z^s$ in (46) and thus find a boundary condition for E_z

$$\frac{\partial E_z}{\partial n} + \left(jk_0 + \frac{1}{2\rho_b}\right) E_z = \frac{\partial E_z^i}{\partial n} + \left(jk_0 + \frac{1}{2\rho_b}\right) E_z^i. \tag{47}$$

A comparison to (22) then reveals that $a(\vec{x}) = jk_0 + 1/2\rho_b$, $b(\vec{x}) = 1$, and $g(\vec{x}) = \partial E_x^i/\partial n + (jk_0 + 1/2\rho_b)E_z^i$, which is a known expression, since the incident field E_z^i is given. We performed two simulations, in each one of which we compared the numerical results regarding the modulus and the phase of the electric field to the analytical solutions [22]. In simulation 1, $a = \lambda_0/2\pi$, and its relative permittivity is $\varepsilon_{\mathrm{r}} = 1 - j4$; the total number of nodes spread in the computational domain is 189. In simulation 2, $a = 0.8\lambda_0/\pi$, and the relative permittivity is $\varepsilon_{\mathrm{r}} = 2.75$, whereas the total number of nodes is 626. These simulations show good concordance when compared to the analytical solutions, as shown in Fig. 8, which plots the solutions along a horizontal line passing through the center of the cylinder.

C. Third Example: TE Scattering

The third example is similar to the second, but takes the TE^z polarization into account. The incident magnetic field is $H_z^i = e^{-jk_0x}$, and the frequency is also 1 GHz. As far as boundary conditions are concerned, the same treatment dispensed to TM^z polarization is employed here; (47) is still valid, but the electric field is substituted by the magnetic field, i.e., $E_z \rightarrow H_z$ and $E_z^i \rightarrow H_z^i$. The difference between the two polarizations lies in the fact that there is a discontinuity in the normal derivative of H_z at the air–dielectric interface, as explained earlier in Section IV. This issue is solved through a subdivision of the computational domain, in which the nodes from one subregion do not influence the nodes from the other, and through a double layer of nodes placed along the interface between these subregions. In this problem, one subregion is the free-space layer between $\partial\Omega$ and ∂S, where [according to (15)] $p(\vec{x}) = \varepsilon_{\mathrm{r}}(\vec{x}) = 1$, whereas the other subregion is the interior of the scatterer (circular region S), where $p(\vec{x}) = \varepsilon_{\mathrm{r}}$. The function $q(\vec{x}) = \mu_{\mathrm{r}}(\vec{x})$ is equal to 1 everywhere. Fig. 9(b) illustrates the test domains from both regions; it is clearly seen that nodes from one side of ∂S do not extend their test domains to the other side. We performed also two simulations. In simulation 1, $a = \lambda_0/2\pi$ and $\varepsilon_{\mathrm{r}} = 4$; the total number of nodes spread throughout the computational domain amounts to 494. In simulation 2, $a = 5\lambda_0/8\pi$ and $\varepsilon_{\mathrm{r}} = 0.25 - j1.75$, whereas the total number of nodes is 759. The concordance between numerical and analytical solutions is again very good, as Fig. 10 indicates. These simulations show that the collocation procedure proved to be quite handy in treating interface conditions.

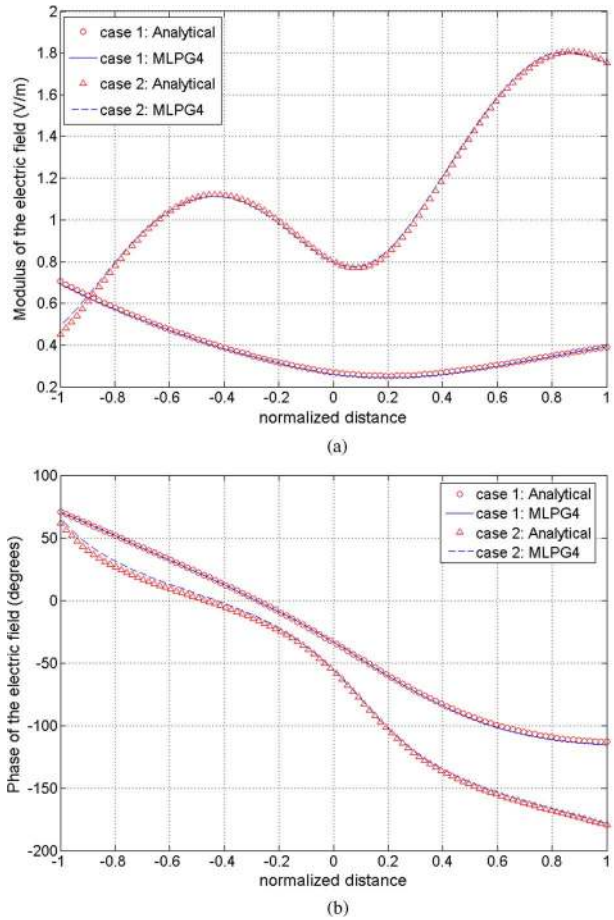

Fig. 8. Second example: (a) amplitude and (b) phase of E_z. The abscissa corresponds to a line in the x-direction passing through the center of the cylinder. The distance is normalized to the cylinder radius a (i.e., distance $= x/a$).

D. Fourth Example: Scattering by Many Objects—The Flow of Light Down a Photonic Crystal

A two-dimensional photonic band-gap crystal is a periodic array of dielectric structures, the most remarkable property of which is that it is able to select what wavelengths can actually propagate through it. This phenomenon can be verified if one sketches the crystal's dispersion curve, from which it can be

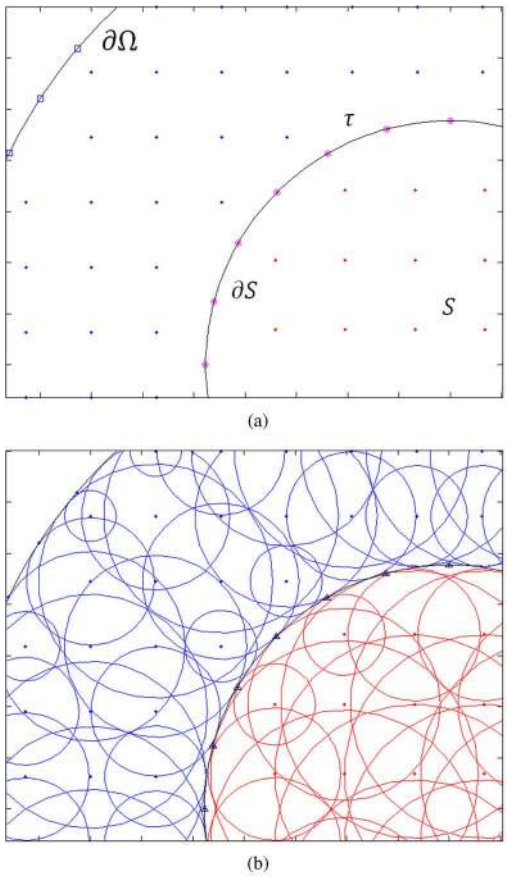

Fig. 9. Portion of the computational domain. (a) Global boundary $\partial\Omega$, the scatterer S, and the scatterer's boundary ∂S, which coincides with the air–dielectric interface τ. Some interior nodes, boundary nodes (three little squares at $\partial\Omega$), and also the double layer of interface nodes (small points at τ) are shown. (b) Profusion of test domains covering the computational domain. The problem is broken up into two subregions: one between $\partial\Omega$ and ∂S, and the other within the scatterer S. Only the interior nodes of both subregions are assigned test domains, which can be seen just touching the interface τ or the global boundary $\partial\Omega$.

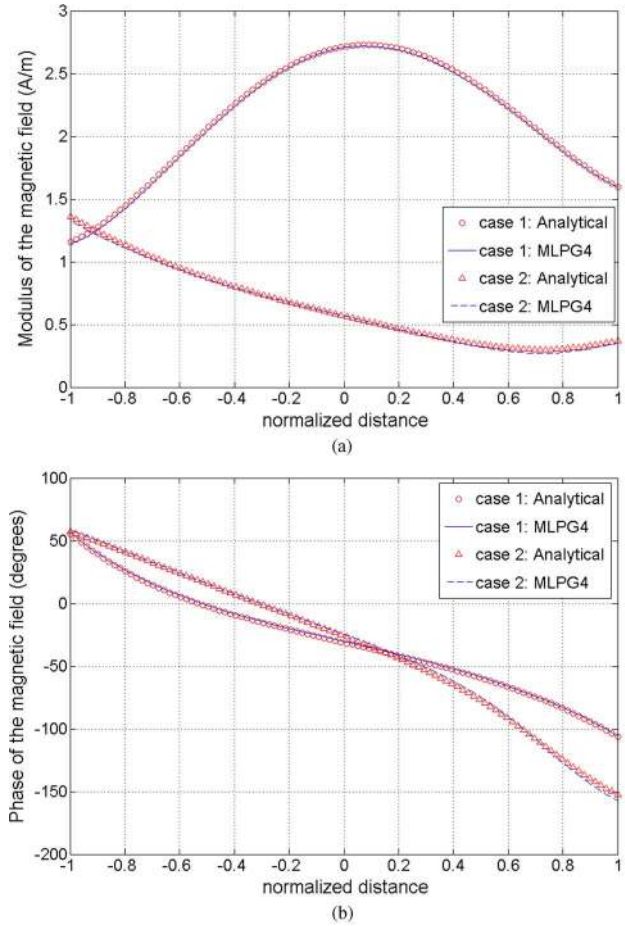

Fig. 10. Third example: (a) amplitude and (b) phase of H_z. The abscissa corresponds to a line in the x-direction passing through the center of the cylinder. The distance is normalized to the cylinder radius a (i.e., distance $= x/a$).

seen that certain wavelengths inside an interval cannot propagate (there are no modes supporting these wavelengths). The "forbidden" wavelengths form a band-gap, i.e., every incoming wave whose wavelength falls inside the band-gap is unable to propagate through the crystal. There is a wide range of applications concerning these photonic band-gap crystals; details about the theory underlying them can be found in [23] and [24].

Let it be a periodic array of dielectric circular rods, whose relative permittivity is $\varepsilon_{\rm r} = 9$, whereas that of the surrounding medium is 1. Each of these rods has a radius r, here normalized to 1. Besides that, the distance between a rod and its neighbor is also r. (It should be kept in mind that this structure is three-dimensional; it is a collection of cylindrical dielectric rods placed side by side, forming a kind of "forest" immersed in a medium where $\varepsilon_{\rm r} = 1$. It is not a planar device such as a microstrip antenna printed on a flat surface. Because no magnitude depends on z, we are concerned here only with the cross section of this structure, whose analysis leads to a two-dimensional problem.) Simulations show that a wave whose wavenumber k_0 is 1 ($k_0 = 2\pi/\lambda_0$) falls within a band-gap, and then is unable to propagate along this structure [25]. Now, given a photonic crystal and an incoming wave unable to propagate through it, if some rods are removed from the structure, forming a path, then this incoming wave will be able to propagate only within the "carved" path. Thus, the incoming lightwave can be guided along a path through the crystal.

The photonic crystal studied in this work has also been analyzed in [25], which employed FEM and another technique (FLAME). Given a periodic structure, we removed some rods, forming an L-shaped path as can be seen in Fig. 11(a), which shows the whole computational domain Ω. We have studied what happens to an incident TM^z plane wave $E_z^i = e^{-jk_0x}$, where $k_0 = 1$, as it impinges upon this structure. The differential equation to be solved is (15), where $p(\vec{x}) = \mu_{\rm r} = 1$ everywhere, $q(\vec{x}) = \mu_{\rm r} = 1$ outside the rods, and $q(\vec{x}) = \mu_{\rm r} = 9$ inside each rod. According to [25] and [26], for band-gap operation and in order to eliminate errors due to imperfect absorbing boundary conditions, Dirichlet conditions corresponding to the incident field are imposed on the whole global boundary (i.e., $E_z(x,y) = E_z^i(x,y) = e^{-jk_0x}$ on $\partial\Omega$). Fig. 11(b) shows the real part of the electric field along the dashed line in Fig. 11(a). The concordance between the results provided by LBIE/MLPG4 and FEM is excellent. Nevertheless, according to [26], FEM uses more than 100 000 degrees of freedom (DoF) to attain this result, whereas our meshless

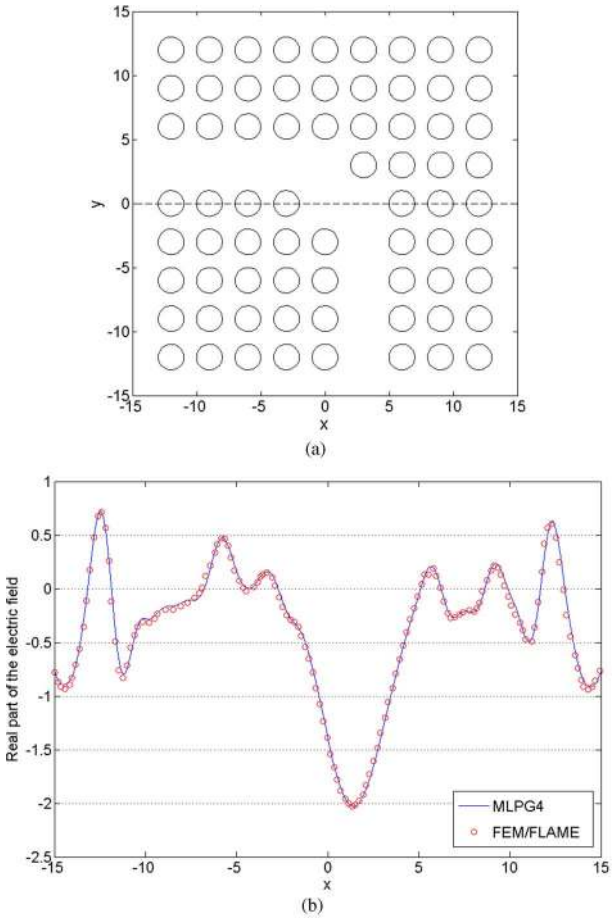

Fig. 11. (a) Photonic crystal, with some rods removed, forming an L-shaped path. (b) Real part of the electric field along the line $y = 0, (-15 \leq x \leq 15)$.

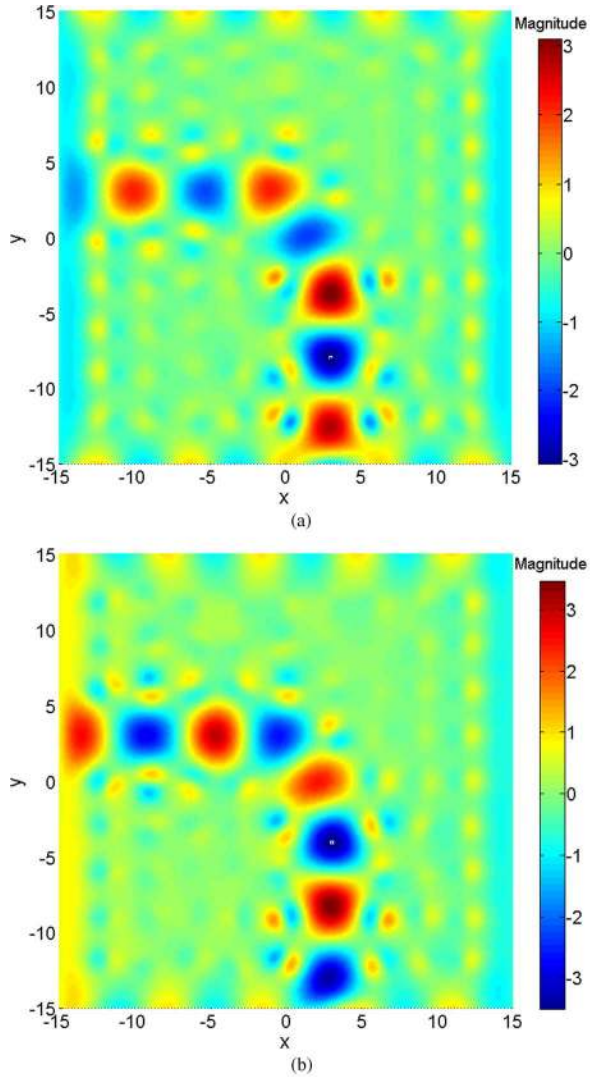

Fig. 12. MLPG4 numerical results for the electric field throughout the whole computational domain Ω. (a) Real part. (b) Imaginary part. It can be observed that the light propagates only within the path formed by removed rods.

method uses 2700 DoF (1 DoF per node). Fig. 12 shows the real and imaginary parts of the electric field across the whole computational domain, where the bending of the flow of light can clearly be observed. The incoming wave whose wavenumber $k_0 = 1$ enters the crystal through the "carved" path formed by the removed rods. Once there, the only way available for this wave is to follow this path until the end, as it cannot "leak" into the bulk of the crystal, because in this region there are no conditions for propagation (the wavenumber $k_0 = 1$ falls within a band-gap). Thus, the photonic crystal described here is able to bend the flow of light in 90° in a completely lossless way (the dielectric rods do not absorb radiation since they are lossless). There is a great resemblance between Fig. 12(b) and [25, Fig. 17], both depicting the imaginary part of E_z throughout the computational domain.

VIII. Conclusion

In this paper, we had the opportunity to illustrate the application of MLPG4/LBIE to a myriad of problems concerning the propagation and scattering of electromagnetic waves. Problems involving radiation boundary conditions, collocation procedures, material discontinuities, excitation by current sources, and scattering by multiple objects have all been addressed with detail. The approach herein presented is such that numerical integrations are required for interior nodes only. Special collocation schemes have been shown to be able to accurately deal with boundary and interface conditions. Better results can be attained by increasing the number of nodes or refining the numerical integrations in each test domain. MLPG4/LBIE somehow resembles FEM in what regards the operation with weak forms and the sparse global matrices; the only major difference is the absence of a mesh. Finally, we can say that this paper succeeded in its task of introducing LBIE to wave scattering analysis. We expect that the insights and the experience drawn from this work could serve as a source of information for future research.

References

[1] G. R. Liu, *Mesh Free Methods: Moving Beyond the Finite Element Method*, 2nd ed. Boca Raton, FL: CRC Press, 2010.

[2] L. Proekt and I. Tsukerman, "Method of overlapping patches for electromagnetic computation," *IEEE Trans. Magn.*, vol. 38, no. 2, pp. 741–744, Mar. 2002.

[3] C. Lu and B. Shanker, "Generalized finite element method for vector electromagnetic problems," *IEEE Trans. Antennas Propag.*, vol. 55, no. 5, pp. 1369–1381, May 2007.

[4] T. Strouboulis, K. Copps, and I. Babuska, "The design and analysis of the generalized finite element method," *Comput. Methods Appl. Mech. Eng.*, vol. 181, pp. 43–69, 2000.
[5] G. Parreira, E. Silva, A. Fonseca, and R. Mesquita, "The element-free Galerkin method in three-dimensional electromagnetic problems," *IEEE Trans. Magn.*, vol. 42, no. 4, pp. 711–714, Apr. 2006.
[6] O. Bottauscio, M. Chiampi, and A. Manzin, "Element-free Galerkin method in eddy-current problems with ferromagnetic media," *IEEE Trans. Magn.*, vol. 42, no. 5, pp. 1577–1584, May 2006.
[7] A. Manzin and O. Bottauscio, "Element-free Galerkin method for the analysis of electromagnetic-wave scattering," *IEEE Trans. Magn.*, vol. 44, no. 6, pp. 1366–1369, Jun. 2008.
[8] S. Atluri and S. Shen, "The meshless local Petrov–Galerkin method: A simple and less-costly alternative to the finite-element and boundary element methods," *Comput. Model. Eng. Sci.*, vol. 3, no. 1, pp. 11–51, 2002.
[9] A. Fonseca, S. Viana, E. Silva, and R. Mesquita, "Imposing boundary conditions in the meshless local Petrov-galerkin method," *Sci. Meas. Technol.*, vol. 2, p. 387, 2008.
[10] D. Soares, Jr., "Numerical modeling of electromagnetic wave propagation by meshless local Petrov–Galerkin formulations," *Comput. Model. Eng. Sci.*, vol. 50, no. 2, pp. 97–114, 2009.
[11] Y. Yu and Z. Chen, "Towards the development of an unconditionally stable time-domain meshless method," *IEEE Trans. Microw. Theory Tech.*, vol. 58, no. 3, pp. 578–586, Mar. 2010.
[12] Y. Yu and Z. Chen, "A 3-D radial point interpolation method for meshless time-domain modeling," *IEEE Trans. Microw. Theory Tech.*, vol. 57, no. 8, pp. 2015–2020, Aug. 2009.
[13] W. Nicomedes, R. Mesquita, and F. Moreira, "A local boundary integral equation (LBIE) method in 2D electromagnetic wave scattering, and a meshless discretization approach," in *Proc. SBMO/IEEE MTT-S Int. Microw. Optoelectron. Conf.*, 2009, pp. 133–137.
[14] W. Nicomedes, R. Mesquita, and F. Moreira, "The unimoment method and a meshless local boundary integral equation (LBIE) approach in 2D electromagnetic wave scattering," in *Proc. SBMO/IEEE MTT-S Int. Microw. Optoelectron. Conf.*, 2009, pp. 514–518.
[15] W. Nicomedes, R. Mesquita, and F. Moreira, "Calculating the band structure of photonic crystals through the meshless local Petrov–Galerkin (MLPG) method and periodic shape functions," *IEEE Trans. Magn.*, vol. 48, no. 2, pp. 551–554, Feb. 2012.
[16] W. Nicomedes, R. Mesquita, and F. Moreira, "A meshless local Petrov–Galerkin method for three dimensional scalar problems," *IEEE Trans. Magn.*, vol. 47, no. 5, pp. 1214–1217, May 2011.
[17] W. Nicomedes, R. Mesquita, and F. Moreira, "Meshless local Petrov–Galerkin (MLPG) methods in quantum mechanics," *Int. J. Comput. Math. Elect. Eng.*, vol. 30, no. 6, pp. 1763–1776, 2011.
[18] Q. Li, S. Shen, Z. Han, and S. Atluri, "Application of meshless Petrov–Galerkin (MLPG) to problems with singularities, and material discontinuities, in 3-D elasticity," *Comput. Model. Eng. Sci.*, vol. 4, no. 5, pp. 571–585, 2003.
[19] Y. Liu and T. Belytchko, "A new support integration scheme for the weak form in meshfree methods," *Int. J. Numer. Methods Eng.*, vol. 82, no. 6, pp. 699–715, May 2010.
[20] D. G. Duffy, *Green's Functions With Applications*. London, U.K.: Chapman & Hall/CRC, 2001.
[21] J. Jin, *The Finite Element Method in Electromagnetics*. New York: Wiley, 1993.
[22] C. Balanis, *Advanced Engineering Electromagnetics*. New York: Wiley, 1989.
[23] J. D. Joannopoulos, S. G. Johnson, J. N. Winn, and R. D. Meade, *Photonic Crystals: Molding the Flow of Light*. Princeton, NJ: Princeton Univ. Press, 2008.
[24] M. Skorobogatyi and J. Yang, *Fundamentals of Photonic Crystal Guiding*. Cambridge, NJ: Cambridge Univ. Press, 2009.
[25] I. Tsukerman, "Electromagnetic applications of a new finite difference calculus," *IEEE Trans. Magn.*, vol. 41, no. 7, pp. 2206–2225, Jul. 2005.
[26] I. Tsukerman, *Computational Methods for Nanoscale Applications, Nanostructure Science and Technology Series*. New York: Springer, 2008.

Williams L. Nicomedes received the Bachelor's and Master's degrees in electrical engineering from the Federal University of Minas Gerais (UFMG), Belo Horizonte, Brazil, in 2008 and 2011, respectively, and is currently pursuing the Ph.D. degree at UFMG, exploring the application and development of meshfree methods in the numerical simulation of photonic crystals and in other areas of applied mathematics.

Renato Cardoso Mesquita was born in Belo Horizonte, Brazil, in 1959. He received the B.S. and M.S. degrees in electrical engineering from the Federal University of Minas Gerais, Belo Horizonte, Brazil, in 1982 and 1986, respectively, and the Dr. degree in electrical engineering from the Federal University of Santa Catarina, Florianópolis, Brazil, in 1990.

Since 1983, he has been with the Department of Electrical Engineering, Federal University of Minas Gerais, where he is currently an Associate Professor. His main research interest is in the area of electromagnetic field computation. He has authored or coauthored over 150 journal and conference papers in this area.

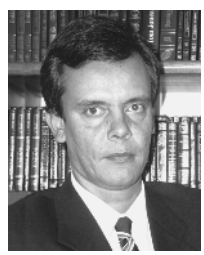

Fernando José da Silva Moreira (S'89–M'98) was born in Rio de Janeiro, Brazil, in 1967. He received the B.S. and M.S. degrees in electrical engineering from the Catholic University, Rio de Janeiro, Brazil, in 1989 and 1992, respectively, and the Ph.D. degree in electrical engineering from the University of Southern California, Los Angeles, in 1997.

Since 1998, he has been with the Department of Electronics Engineering, Federal University of Minas Gerais, Belo Horizonte, Brazil, where he is currently an Associate Professor. His research interests are in the areas of electromagnetics, antennas and propagation. He has authored or coauthored over 100 journal and conference papers in these areas.

Dr. Moreira is a member of Eta Kappa Nu and the Brazilian Microwave and Optoelectronics Society.